Chemical Engineering Journal 486 (2024) 150136

Contents lists available at ScienceDirect

Chemical Engineering Journal

journal homepage: www.elsevier.com/locate/cej

# High performance flow-focusing droplet microreactor. Extractive separation of rare earths as case of study

Christian Fernández-Maza, Gloria González-Lavín, Lucía Gómez-Coma, Marcos Fallanza, Inmaculada Ortiz *

*Departamento de Ingenierías Química y Biomolecular, Universidad de Cantabria, Av. Los Castros s/n, 39005 Santander, Spain*

ARTICLE INFO

*Keywords:*
Flow-focusing microreactor
Droplet generation
Rare earths microextraction
CFD modelling
Multiphase reaction

ABSTRACT

This work advances the knowledge of the design and manufacture of microdroplet reactors for reactive liquid–liquid systems assisted by advanced simulation techniques (CFD). The mathematical model is based on the integrated analysis of the fluid dynamics for multiphase systems, passive mixing of reactants inside and outside the microdroplet and interfacial reaction rate. To validate the results obtained with the predictive model a spiral microdevice with droplet generation using flow-focusing geometry has been designed and fabricated by additive manufacturing. First, the influence of fluid flowrate, hold-up and viscosity on the droplets frequency and size has been evaluated with the model and assessed experimentally. Next, the performance in the separation of a binary Dysprosium-Lanthanum system has been tested, working with a dispersed aqueous phase containing the rare earth elements (REEs) solution and a continuous organic phase constituted of a solution of the extractant Cyanex® 572 in Shellsol® D70. The extraction experiments have been conducted at residence times between 3 and 60 s to generate aqueous phase monodispersed droplets with high interfacial area that varies between 61.4 and 49.2 $cm^2 \cdot cm^{-3}$ depending on the operating conditions. At pH 1, 90 % of dysprosium has been extracted, and almost complete separation of both REEs has been achieved. Very good agreement between simulated and experimental results has been reached with an error lower than 12 %. Therefore, here we provide the tools to design and predict the microdroplet enhanced performance of extractive liquid–liquid microreactors.

## 1. Introduction

The world today is experiencing a catastrophic situation caused by the COVID-19 pandemic and the subsequent Russian invasion of Ukraine. This has caused a global crisis due to a major disruption of the supply chain and manufacturing capacity. Product shortages have led to an uncontrolled increases in the price of materials and energy [1]. For this reason, it is important to make progress in the development and application, whenever possible, of technologies with low operating costs, easy and cheap to manufacture and with low reagents consumption, characteristics covered by microfluidics. This technology is at its peak due to i) its high capability to precisely control the concentration of molecules in the space and time, leading to a high interest in several fields involving two-phase systems, ii) its high surface-to-volume ratio, which favours mass and heat transport between phases [2,3], iii) mixing phenomena are also limited by diffusion and secondary flows [4]. This transport capacity, together with reduced and highly controlled residence times, has been reported to play a key role in suppressing the development of undesirable secondary reactions in complex reactive systems, favouring higher selectivity and yields [5].

Microfluidic devices are found in a wide range of configurations handling single-phase and multiphase fluid flows. The formers are often used as micromixers or microreactors to perform homogeneous reactions [4]. Gomez-Pastora et al. [2] reported the in-depth analysis of the influence of operational and geometric variables on the performance of microfluidic separation microdevices with two homogeneous fluid phases. Furthermore, multiphase flows have been documented in microfluidic devices for liquid–liquid [6], gas–liquid [7] and solid–liquid [8] mixtures and have been used in several fields for different applications: in medicine, to development of technology that facilitates the precise molecular diagnosis of heterogeneous cancer specimens, allowing the selection of patients for specific cancer therapies [9]; in polymerization, the use of microreactors to increase the rate and molecular weight in continuous enzymatic polymerization compared to the use of batch reactors [10]; in electrocatalytic oxidation, improving the

* Corresponding author.
*E-mail address:* ortizi@unican.es (I. Ortiz).

https://doi.org/10.1016/j.cej.2024.150136
Received 18 September 2023; Received in revised form 19 February 2024; Accepted 1 March 2024
Available online 11 March 2024

**Nomenclature**

*Roman symbols*

| | |
|---|---|
| $A$ | interfacial area ($cm^2 \cdot cm^{-3}$) |
| $a$ | radius of the droplet in the $x$ direction (cm) |
| $b$ | radius of the droplet in the $y$ direction (cm) |
| $c$ | radius of the droplet in the $z$ direction (cm) |
| $C_j$ | molar concentration of species $j$ ($kmol \cdot m^{-3}$) |
| $C_j^0$ | initial molar concentration of species $j$ ($kmol \cdot m^{-3}$) |
| $De$ | Dean number (-) |
| $d_h$ | hydraulic diameter of the micro-channel (m) |
| $D_{i.q}$ | mass diffusion coefficient for species $i$ in the phase $q$ ($m^2 \cdot s^{-1}$) |
| $E$ | percentage of rare earth extraction (-) |
| $\vec{g}$ | acceleration of gravity ($m \cdot s^{-2}$) |
| $\vec{j}^{\,i}$ | diffusion flux of species $i$ ($kg \cdot m^{-2} \cdot s^{-1}$) |
| $k_b$ | kinetic constant of the reverse chemical reaction ($s^{-1}$) |
| $K_c$ | equilibrium constant (-) |
| $k_f$ | kinetic constant of the direct chemical reaction ($s^{-1}$) |
| $M_w^i$ | molecular weight of species $i$ ($kg \cdot kmol^{-1}$) |
| $N_d$ | total number of droplets inside the microdevice (-) |
| $p$ | pressure ($kg \cdot m^{-1} \cdot s^{-2}$) |
| $Q_{Aq}$ | flow rate of the aqueous phase ($ml \cdot min^{-1}$) |
| $Q_{Org}$ | flow rate of the organic phase ($ml \cdot min^{-1}$) |
| $\mathscr{R}$ | net rate of production of species $i$ by interfacial chemical reaction ($kg \cdot m^{-3} \cdot s^{-1}$) |
| $r_c$ | curvature radius of the micro-channel (m) |
| $Re$ | Reynolds number (-) |
| $REE$ | Rare Earth Element (-) |
| $t$ | time (s) |
| $\vec{v}$ | velocity ($m \cdot s^{-1}$) |
| $V_{Aq}$ | total volume of aqueous phase ($cm^3$) |
| $V_{Org}$ | total volume of organic phase ($cm^3$) |
| $Y^i$ | mass fraction of species $i$ (-) |

*Greek symbols*

| | |
|---|---|
| $\alpha$ | volume fraction (-) |
| $\beta$ | separation factor (-) |
| $\varepsilon$ | enhancement factor ($mm^{-1} \cdot min^{-1}$) |
| $\eta_j^{'}$ | kinetic order for reactant species $j$ (-) |
| $\eta_j^{''}$ | kinetic order for product species $j$ (-) |
| $\mu$ | viscosity ($kg \cdot m^{-1} \cdot s^{-1}$) |
| $\nu_i^{'}$ | stoichiometric coefficient for reactant $i$ (-) |
| $\nu_i^{''}$ | stoichiometric coefficient for product $i$ (-) |
| $\rho$ | density ($kg \cdot m^{-3}$) |
| $\sigma$ | surface tension coefficient ($N \cdot m^{-1}$) |
| $\tau$ | residence time (s) |
| $\bar{\bar{\tau}}$ | stress tensor ($kg \cdot m^{-1} \cdot s^{-2}$) |

performance of wastewater treatment and disinfection by combining macro-reactors with electro-microreactors equipped with boron-doped diamond anode, which intensifies mass transport and reduces energy consumption [11]; in catalysis, with the synthesis and immobilization of gold nanoparticles to build catalytic microreactors for the production of fine organic chemicals with high control of reaction parameters [12], or the selective photocatalytic synthesis of benzaldehyde in carbon nitride immobilized microcapillaries [13], among others.

Liquid-liquid extraction is probably one of the separation processes that can benefit most from its synergy with microfluidics, given the small molecular diffusion distances and high surface-to-volume ratios, narrow residence time distributions and well-defined flow conditions, which together support a controlled process operation with uniform conditions and accurate results [14]. In addition, the geometry of the microchannels is crucial, as the incorporation of curved parts induces passive mixing through inertial, centripetal, and viscous forces, creating a secondary motion perpendicular to the main flow direction, known as Dean vortices, which increases the mixing efficiency and consequently the mass transfer performance in the microdevice [4,15]. There are different ways to operate with two fluid phase systems: i) flowing both liquid phases in parallel flow, for instance with Y-Y shape microdevices, which is very interesting to perform liquid–liquid microextractions in a simple way [16], but has the smallest contact area between phases, ii) with jet-flow regime [17] or, iii) generating a dispersed phase with liquid droplets. The latter presents a high potential due to the high surface area to volume ratio, shorter diffusion distances and reduced mass transport time that result in faster reactions [18] and justify the use of these systems in research over more conventional microscale reactors or miniaturized dispersive continuous flow microfluidic devices.

Droplet generation is achieved by either active or passive methods. Active methods make use of external forces (electrical, magnetic, thermal or mechanical) to stimulate droplet formation, while passive, pressure-driven methods rely on the geometric design of the microchannel junction where the dispersed and continuous phases are in contact [19]. Depending on the junction structure, three main methods of passive droplet generation emerge: co-flow, cross-flow and flow-focusing.

The co-flow configuration has two aligned inlets that allow the fluids to flow in a parallel direction. It was first implemented in microfluidics by Cramer et al. in 2004 [20], who inserted an inlet microcapillary into a rectangular flow cell. This geometry was often created by inserting a tapered cylindrical glass tube aligned into a rectangular or square glass capillary [20]. By modifying the operating conditions, it is possible to generate different fluid dynamic regimes, generating a dispersed phase jet or droplets with different size. Fabrication of these geometries is not straightforward and is not appropriate when the phases have significantly different densities.

In the cross-flow category, the dispersed and continuous phases meet at an angle in the range $0^\circ < \theta < 180^\circ$, with the T-junction ($\theta = 90^\circ$) being the most common structure [21]. Thorsen et al. [22] were the first authors to use a microdevice with this configuration in 2001 to generate water-in-oil droplets to produce ordered dynamic patterns in pressure controlled laminar flows. In these microdevices two phases flow through two orthogonal channels and form droplets on contact. They are widely used because of their simplicity and ability to produce monodispersed droplets [21]. The size of the droplets can be modified by changing the fluid flow rates, the dimensions of the channels or changing the relative viscosity between the two phases [18]. The weakness of these devices lies in the asymmetric geometry, which causes the generation of off-centre droplets.

The flow-focusing geometry is widely used to generate monodispersed droplets and was first proposed in 2003 by Anna et al. [23]. In this geometry, the dispersed phase is squeezed between two streams of the continuous phase and then breaks up to form droplets. In the dripping regime, the thread expands sharply at the very outlet of the nozzle, and the interfacial tension forces the head of the thread to become spherical in shape. The sudden expansion leads to deceleration and stagnation of the tip and viscous drag of the continuous fluid. At low Reynolds numbers, the viscous drag on the emerging droplet stretches and reduces the thickness of the neck, causing it to break and generate the droplet [24].

Due to the symmetric shear stress exerted by the continuous phase on the dispersed one [25,26], the flow-focusing configuration promotes more controlled and more stable droplet generation compared to the

cross-flow configuration, and the fabrication of these devices is simpler than using a co-flow geometry. The characteristics of microfluidic droplet generation position this configuration as a promising alternative in the analysis of separation processes based on two fluid phase solvent extraction, more specifically here, the separation of rare earth elements (REEs). These elements are key critical materials to ensure the current and future technological development [27] and their separation is extremely complex, having been reported as one of the seven separations that could change the world [28]. The advantages of microfluidics allow efficient testing of different separation agents, while helping to determine critical parameters (kinetic parameters) for process design.

Previously, Nichols et al. [29] carried out the extraction of REEs in a simple straight microdevice are reported a microfluidic method to measure the kinetics of metal ion extraction. These experimental results were successfully modelled by Zhang et al. [30] using computational fluid dynamics (CFD) techniques with fitting parameters (kinetic constants) and centrosymmetric simplifications in a T-junction cylinder geometry, in order to understand the characteristics of lanthanide droplet-based extraction.

This work addresses for the first time the modelling and experimental validation of the heterogeneous microextraction of two rare earth elements in a 3D spiral geometry with droplet generation, deepening on the coupling between mass transfer phenomena and passive mixing. In a device with flow of a continuous organic phase and dispersed aqueous microdroplets, the curved parts of the microdevice are key to achieve efficient passive mixing in the continuous phase, which together with the vortices generated inside the droplets increase the efficiency of the extraction process (Fig. 1). Furthermore, the mathematical model that considers gravitational and centripetal forces is capable of predicting the mixing and mass transfer of both phases, constituting the most advanced tool to date for the analysis of separation processes. This model is able to describe the coupling between mass transport phenomena and passive mixing on the microscale allowing to quantify the importance of the microdevice geometry in the performance of this type of separation. In this way, the extraction of rare earths (dysprosium and lanthanum) using a selective extractant (Cyanex® 572) with microdroplet generation under different operating conditions has been used as a case study due to its particular industrial interest [31].

## 2. Mathematical model

In order to quantify the solute's concentration at each point in the microfluidic device, and then evaluate the performance of the microfluidic rare earth extraction, the flow field, coupled with the mass transport and chemical reaction equations must be solved. In this work, the Navier-Stokes equations for multiphase, incompressible, and dynamic state laminar flow in microfluidic devices have been solved to predict the fluid dynamics of droplet generation with flow-focusing configuration, Eqs. (1)-(4); in addition, the transport of species with reactive solvent extraction in a heterogeneous liquid–liquid system, Eqs. (5)-(7), has been included.

The conservation of mass inside the microdevice is described by the continuity equation for each phase. For phase "$q$" it can be written as follows:

$$\frac{\partial}{\partial t}\left(\alpha_q\,\rho_q\right)+\nabla\cdot\left(\alpha_q\,\rho_q\,\vec{v}_q\right)=0 \tag{1}$$

where "$\rho_q$" is the density (kg·m$^{-3}$) and "$\vec{v}_q$" the velocity (m·s$^{-1}$) of the phase "$q$". The volume fraction describes the space occupied by each phase, and the laws of conservation of mass and momentum are satisfied by each phase independently. "$\alpha_q$" is the volume fraction of the phase "$q$".

The equation describing the non-relativistic momentum transport within the microdevice for the phase "$q$" is:

$$\frac{\partial}{\partial t}\left(\alpha_q\,\rho_q\,\vec{v}_q\right)+\nabla\cdot\left(\alpha_q\,\rho_q\,\vec{v}_q\,\vec{v}_q\right)=-\alpha_q\,\nabla\,p+\nabla\cdot\bar{\bar{\tau}}_q+\alpha_q\,\rho_q\,\vec{g} \tag{2}$$

where "$p$" is the pressure (kg·m$^{-1}$·s$^{-2}$), "$\vec{g}$" is the acceleration of gravity (m·s$^{-2}$), and "$\bar{\bar{\tau}}_q$" is the stress tensor (kg·m$^{-1}$·s$^{-2}$) that is given by:

$$\bar{\bar{\tau}}_q=\mu_q\left[\alpha_q\left(\nabla\vec{v}_q+\nabla\vec{v}_q^{\,T}\right)+\frac{2\alpha_q}{3}\nabla\cdot\vec{v}_q\,\bar{\bar{I}}\right] \tag{3}$$

The shape of the liquid–liquid interface in a heterogeneous system may be described as:

$$p_2-p_1=\sigma\left(\frac{1}{R_1}+\frac{1}{R_2}\right) \tag{4}$$

where "$p_1$" and "$p_2$" are the pressures (kg·m$^{-1}$·s$^{-2}$) in the two fluids on either side of the interface, "$R_1$" and "$R_2$" are two radii in orthogonal directions (m), and the surface tension coefficient "$\sigma$" was experimentally determined at 20 °C using the method of the Axisymmetric Drop Shape Analysis (ADSA).

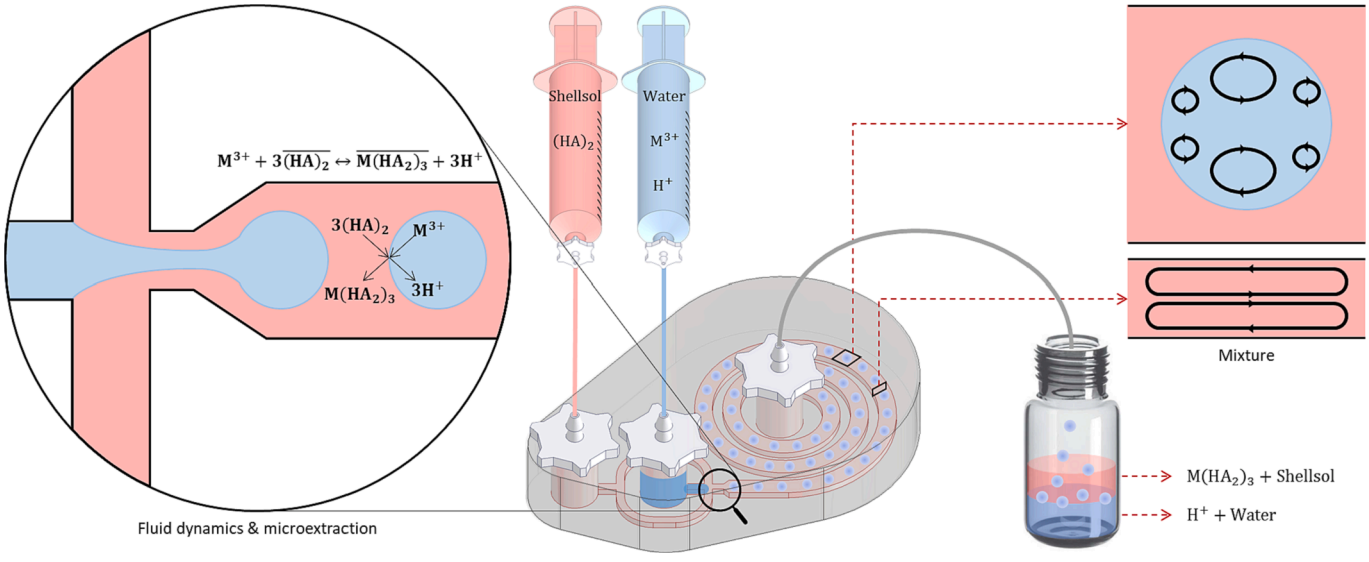


**Fig. 1.** Schematic diagram of the fluid dynamics and microextraction of REE "$M^{3+}$" analysis, using Cyanex® 572 extractant "$(HA)_2$" in the microfluidic device with flow-focusing droplet generation.

**Table 1**
Value of parameters employed in the computational model.

| Components of the aqueous phase | Molecular weight ($kg{\cdot}kmol^{-1}$) | Components of the organic phase | Molecular weight ($kg{\cdot}kmol^{-1}$) |
|---|---|---|---|
| $Dy^{3+}$ (Dysprosium) | 162.5 [a] | $Dy(HA_2)_3$ | 1089.5 |
| $La^{3+}$ (Lanthanum) | 138.9 [a] | $La(HA_2)_3$ | 1065.5 |
| $H^+$ (Proton) | 1.01 [a] | $HA_2$ (Cyanex® 572) | 310 [b] |
| $H_2O$ (Water) | 18.02 [a] | Shellsol® D70 | 174 [c] |

| **Parameter** | **Aqueous phase** | **Organic phase** |
|---|---|---|
| Density ($kg{\cdot}m^{-3}$) | 998.2 [a] | 796 [c] |
| Viscosity ($kg{\cdot}m^{-1}{\cdot}s^{-1}$) | $1.00{\cdot}10^{-3}$ [a] | $1.60{\cdot}10^{-3}$ [c] |
| Diffusion coefficient of $Dy^{3+}$ ($m^2{\cdot}s^{-1}$) | $5.82{\cdot}10^{-10}$ [e] | $2.00{\cdot}10^{-10}$ [d] |
| Diffusion coefficient of $La^{3+}$ ($m^2{\cdot}s^{-1}$) | $6.19{\cdot}10^{-10}$ [e] | $1.98{\cdot}10^{-10}$ [d] |
| Surface tension coefficient ($N{\cdot}m^{-1}$) | – | $9.61{\cdot}10^{-3}$ [f] |
| Equilibrium constant (-) | – | 1.54 [f] |

[a] [32], [b] [33], [c] [34], [d] (Estimated by Wilke-Chang [35]), [e] [36], [f] (Experimental).

It is possible to describe the mixing and transport of chemical species by solving the conservation equations describing convection, diffusion transport and reaction sources for each component. The generalised species transport equation, when applied to a fluid–fluid multiphase system is:

$$\frac{\partial}{\partial t}\left(\alpha_q\ \rho_q\ Y_q^i\right) + \nabla\cdot\left(\alpha_q\ \rho_q\ \vec{v}_q\ Y_q^i\right) = -\nabla\cdot\alpha_q\ \vec{J}_q^{\,i} + \mathscr{R} \tag{5}$$

where "$Y_q^i$" is the mass fraction of the species "$i$", "$\vec{J}_q^{\,i}$" is the diffusion flux ($kg{\cdot}m^{-2}{\cdot}s^{-1}$) of species "$i$" which arises due to its concentration gradient and "$\mathscr{R}$" is the formation/disappearance ($kg{\cdot}m^{-3}{\cdot}s^{-1}$) of components "$i$" at the interphase ($0 < \alpha_q < 1$) due to the heterogeneous chemical reactions. Using Fick's law, it is possible to describe the mass diffusion flux of species "$i$" as a function of the concentration gradient in each phase "$q$":

$$\vec{J}_q^{\,i} = -\rho_q\ D_{i,q}\ \nabla\ Y_q^i \tag{6}$$

here "$D_{i,q}$" is the mass diffusion coefficient ($m^2{\cdot}s^{-1}$) for species "$i$" in the phase "$q$".

$$\mathscr{R} = M_w^i\left(\nu_i^{''} + \nu_i^{'}\right)\left(k_f\prod_{j=i}^{N}\left[C_j\right]^{\eta_j^{'}} - k_b\prod_{j=i}^{N}\left[C_j\right]^{\eta_j^{''}}\right);\qquad K_c = \frac{k_f}{k_b} \tag{7}$$

where "$M_w^i$" ($kg{\cdot}kmol^{-1}$) is the molecular weight of the species "$i$"; "$\nu_i^{''}$" and "$\nu_i^{'}$" are the stoichiometric coefficients of the products and reagents for the species "$i$"; "$k_f$" and "$k_b$" are the kinetic constants ($s^{-1}$) of the direct and reverse chemical reactions; "$K_c$" is the equilibrium constant that has been obtained experimentally as shown in the "Extraction equilibrium of rare earths" subsection; "$C_j$" is the molar concentration ($kmol{\cdot}m^{-3}$) of the components "$j$" in the interphase; and "$\eta_j^{''}$" and "$\eta_j^{'}$" are the reaction kinetic orders for products and reagents of the species "$j$".

The boundary conditions at the inlet of the microdevice correspond to the species composition of each phase, the magnitude of the velocity perpendicular to the inlet surfaces and the atmospheric pressure at the outlet of the microdevice. A no-slip boundary condition was assigned to the walls, where the water-wall contact angle was measured experimentally (Liquid-liquid phase properties) and found to be 107° (as shown in Fig. S1), corresponding to the hydrophobic material (PDMS) of the microfluidic device.

The numerical simulation was performed using a finite volume solver, ANSYS Fluent 19.2 (ANSYS, Inc., Canonsburg, PA, USA). A structured grid was defined and applied to discretise the computational domain. To capture the complex flow field in the droplet generation and the location of the interface between the two phases, the geometry was meshed with a regular mesh using a multizone method where the mesh is refined in the radial direction to optimise the computational time.

The chemical reaction is considered to be a very fast interfacial reaction and the progress of the reaction has been solved using a pressure-based approach in pseudo-transient time using the Heterogeneous Stiff Chemistry Solver. The species solution method is first order upwind for the momentum equation and second order upwind for the energy equations.

The set of equations (1)-(7) has been solved in the computational domain established for the geometry of the microdevice. The values of the used parameters in the model are summarised in Table 1.

## 3. Materials and methods

### 3.1. Experimental section

The following reagents were required for the fabrication of the microdevices: acrylonitrile butadiene styrene filament (ABS, Smart materials 3D®), polydimethylsiloxane (PDMS, Sylgard™ 184 silicone elastomer and curing agent, DOW®), acetone (≥99.8 %, Fisher Chemical®) and propan-2-ol (≥99.8 %, Fisher Chemical®).

For the extraction experiments, $DyCl_3{\cdot}6H_2O$ and $LaCl_3{\cdot}7H_2O$ salts were dissolved in 0.001–0.1 M hydrochloric acid solution (37 %, Fisher Chemical®) to obtain an aqueous phase with a composition of 0.68 mM of each REE at different values of pH (1–3). The organic phase was made of 20 % v/v Cyanex® 572 extractant (CYTEC Industries) dissolved in Shellsol® D70 (KREMER®).

### 3.2. Design and manufacture of microfluidic devices

The microchannel has been designed with an Archimedean spiral geometry (can be seen in Fig. S2 in the supplementary material) because it is a good passive mixer due to the generation of secondary flow (Dean vortices) [4]. This three-dimensional geometry has a rectangular cross section (1.2 mm high and 3 mm wide) and a total length of 200 mm (Fig. S2). It has a flow-focusing configuration for droplet generation with two inlets (one for each phase) and one outlet. More information is available in the supplementary material (Fig. S3).

Microdevices were fabricated by a two-step acrylonitrile butadiene styrene (ABS) scaffold removal method to achieve 3D micrometric channels in a single block of PDMS [37]. This method uses additive manufacturing techniques by 3D printing with Fused Filament Fabrication (FFF) technology. First, the channel geometry is designed in Autodesk Inventor® (Fig. 2.a) and all the printing parameters are entered into the Ultimaker Cura® software (Fig. 2.b). The geometry is then printed in a 3D printer (Ultimaker® S3, Fig. 2.c) using a 0.25 mm print core (Ultimaker®) and acrylonitrile butadiene styrene (ABS) filament. The ABS 3D geometry (Fig. 2.d) is laid in a cured PDMS (DOW Sylgard 184®) bed, covered with liquid PDMS (Fig. 2.e), and placed in a

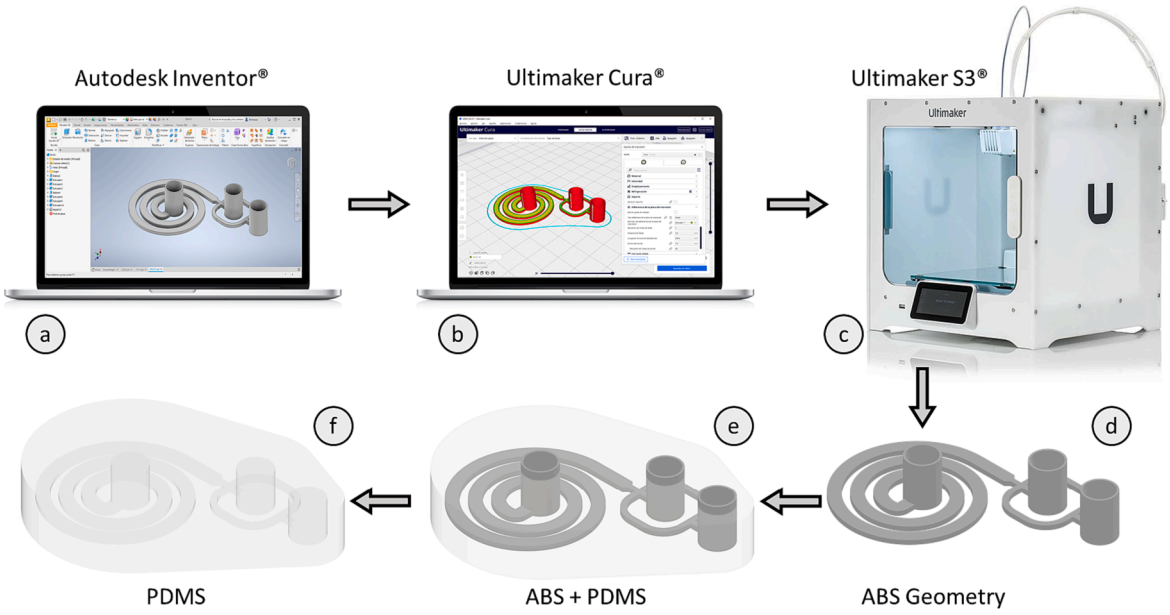


**Fig. 2.** Schematic representation of the polymer scaffold-removal fabrication method for design and manufacturing of microfluidic devices.

vacuum oven (Memmert®) to degas and cure the PDMS (at 60 °C). After that, the scaffold polymer is removed by dissolving with acetone and cleaned by injecting isopropanol, leaving an empty cavity inside the single block of PDMS (Fig. 2.f). The result is a highly precise and completely transparent microdevice, as shown in the supplementary material (Fig. S4).

### 3.3. Liquid-liquid phase properties

The contact angle of PDMS with water was measured experimentally using the Kruss® DSA25S drop shape analyser. A bed of PDMS was cured on the bottom of a glass cuvette, treated with acetone to remove ABS and then cleaned with isopropanol, as it is done in the manufacture of microdevices. To measure the contact angle, the organic phase used in the experiments was previously added to the cuvette with PDMS, the DSA25S syringe was filled with the aqueous phase containing the REE used in the experiment, and a drop of this phase was deposited on the PDMS bed, remaining immersed in the organic phase, as shown in Fig. 3. The sessile drop method is used to measure the contact angle with Kruss® Advance 1.12 software.

### 3.4. Fluid dynamics of droplets generation

For the experimental analysis of the fluid dynamics inside the microdevice, two syringe pumps were used to feed the two phases; one syringe supplied the organic solution, containing the extractant (Cyanex® 572) diluted in Shellsol® D70, while the second syringe pumped the aqueous solution, containing the rare earth elements (dysprosium and lanthanum) and methylene blue (which provides clear visualisation and the ability to accurately measure the shape of the droplets). The syringes were connected to the PDMS microreactor using Tygon® tube by Luer Lock connectors. The flow rate in each experiment was adjusted with both syringe pumps to analyse the droplets generated. The experiments were then carried out at room temperature (22 ± 2 °C) flowing the organic solution as the continuous phase, while W/O (water in oil) droplets of the aqueous solution constituted the dispersed phase. Fig. 4 shows a schematic diagram of the experimental setup.

To analyse the influence of the viscosity variation on the fluid

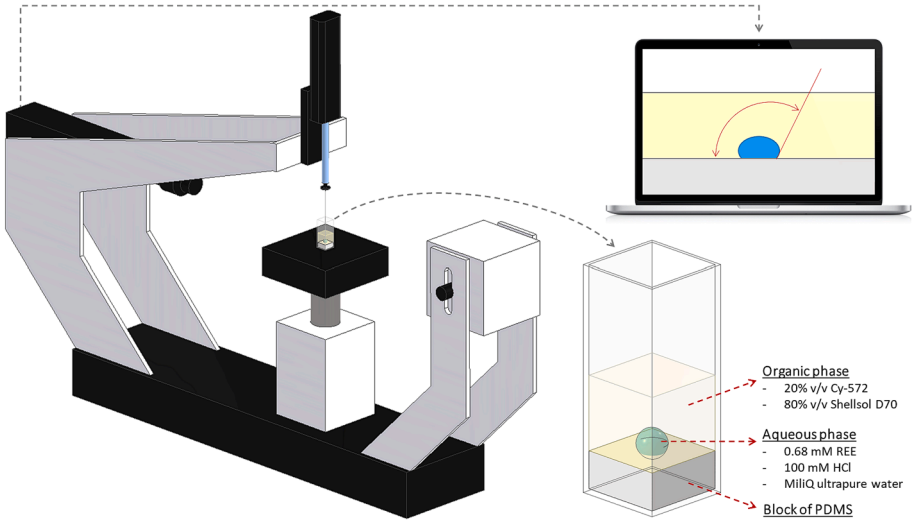


**Fig. 3.** Schematic representation of the method for measuring the contact angle between the PDMS and the aqueous phase immersed in the organic phase.

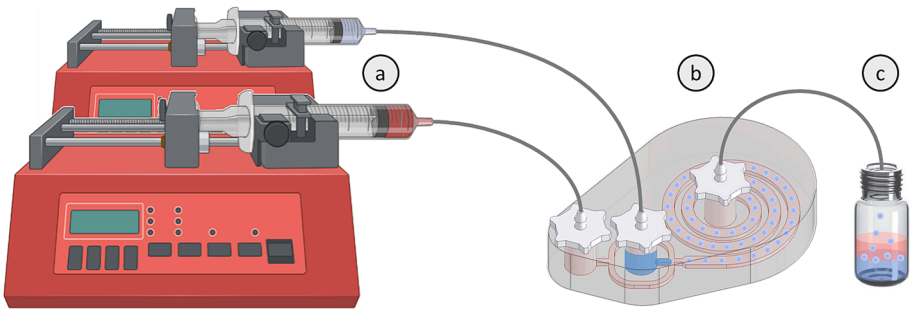


**Fig. 4.** Experimental system for the microextraction composed of a) syringe pumps, b) the microfluidic device and c) the sample vial.

dynamics of the system, while the viscosity of the dispersed phase was kept constant ($\mu_{Aq}$ = 1 cP), the viscosity of the continuous phase was changed in the range of 1 to 7 cP by adding a high-viscosity synthetic oil (initially constituted of 20 % v/v Cyanex® 572 in Shellsol® D70). The amount of added oil was different for each experiment and the exact viscosity of this phase was measured in a Fungilab® Alpha Series viscometer.

### 3.5. Extraction equilibrium of rare earths

The equilibrium constant ($K_c$) of the extraction reaction between dysprosium and the extractant Cyanex® 572 was determined experimentally following a conventional batch contact; 10 ml of aqueous phase ([$M^{3+}$] = 10 to 0.1 mM) were contacted with 10 ml of organic phase (20 % v/v Cy-572 in Shellsol® D70) under stirring. Samples (1 ml of aqueous phase) were taken when equilibrium was reached and the liquid phases were separated by decantation. The REE extraction yield is calculated from the difference between the initial concentration and the concentration of this metal at equilibrium in the aqueous phase. This concentration was measured in the Agilent® 4210 Microwave Plasma-Atomic Emission Spectrometer.

### 3.6. Microfluidic extraction of rare earth elements

For the experimental analysis of the microextractors performance, two syringe pumps were used to feed the reagents; one syringe supplied the organic solution, containing the extractant (Cyanex® 572) while the second syringe pumped the aqueous solution, containing the rare earth elements (dysprosium and lanthanum). The flow rate was adjusted for each experiment (between 0.1 and 12 ml·min$^{-1}$) to generate droplets maintaining a dispersed phase flow rate of 30 % of the total flow rate (AP hold-up) in all extraction experiments. These experiments were then carried out at room temperature (22 ± 2 °C) flowing the organic phase as the continuous one, while W/O droplets of the aqueous solution constituted the dispersed phase.

Fig. 4 represents the experimental system used for REE microextraction. Several samples were taken at different residence times using a decantation method that separates the aqueous phase from the organic one to quench the reaction at the outlet of the microdevice (Fig. 4.c). The aqueous samples were taken with a Pasteur pipette, diluted in ultrapure water and acidified by adding nitric acid. Finally, the concentration of rare earth elements was measured in the MP-AES at a wavelength of 353.2 nm and 408.7 nm for dysprosium and lanthanum, respectively. The percentage of rare earth extraction ($E$) by Cyanex® 572 was calculated from the concentration values as:

$$E = \frac{C^0_{M^{3+}} - C_{M^{3+}}}{C^0_{M^{3+}}} \tag{8}$$

where "$C^0_{M^{3+}}$" is the original metal ion concentration (kmol·m$^{-3}$) in the aqueous phase before the extraction and "$C_{M^{3+}}$" the metal ion concentration in the aqueous medium (kmol·m$^{-3}$) after extraction.

## 4. Results and discussion

### 4.1. Hydrodynamics

The analysis of the operating variables, i.e., flow rate, hold-up and viscosity of the fluid phases, on the fluid dynamics of the system was carried out. To this end, a set of experiments was designed using the dye methylene blue in the dispersed phase (aqueous phase) to trace the droplet generation in terms of frequency and size of the droplets. In the microfluidic device with flow-focusing geometry, as the inlet flow rates increase (residence time decreases), while maintaining a 30 % of hold-up of the aqueous phase (flow rate of the aqueous phase with respect to the total flow rate, Eq. (9)), the characteristics of the generated droplets are affected, resulting in smaller droplets and consequently, in an increase in the frequency of droplet generation.

$$AP\ hold-up = \frac{Q_{Aq}}{Q_{Aq} + Q_{Org}} \cdot 100 \tag{9}$$

where "$Q_{Aq}$" and "$Q_{Org}$" are the flow rate (ml·min$^{-1}$) of the aqueous phase and the organic phase, respectively.

For the flow-focusing configuration, the geometries of the microdevice channel produce ellipsoidal droplets (spheres flattened at the top and bottom), as shown in the 3D simulation in Fig. 5. In this way, the interfacial area of the droplets inside the microdevice varies between 61.4 and 49.2 cm$^2$·cm$^{-3}$ over the range of the studied operating conditions (residence times from 3 to 60 s), calculated as the surface area of all droplets divided by the volume of the aqueous phase in the microdevice, according to the following equation:

$$A = \frac{4\pi\left(\frac{a^p b^p + a^p c^p + b^p c^p}{3}\right)^{\frac{1}{p}} \cdot N_d}{V_{Aq}} \tag{10}$$

where "$p$" has a value of 1.6, "$a$", "$b$", and "$c$" represent the radius of the droplet (cm) in the x, y, and z directions of the system respectively, "$N_d$" is the total number of droplets inside the microdevice and "$V_{Aq}$" is the total volume of aqueous phase (cm$^3$) inside the microdevice.

Fig. 6 shows a comparison between the results obtained with CFD simulations (left part of the figure) and the experiments carried out with the blue dye (on the right). In both cases, under the same operating conditions ($Q_{Aq}$ = 0.429 ml·min$^{-1}$, $Q_{Org}$ = 1 ml·min$^{-1}$, $\tau$ = 30 s, $\mu_{Aq}$ = 1 cP, $\mu_{Org}$ = 1.6 cP) a droplet generation frequency of 1.67 ± 0.07 droplets·s$^{-1}$ was obtained (1.7 droplets·s$^{-1}$ in CFD simulations), with droplets of spherical shape flattened at the top and bottom with a diameter of 2.43 ± 0.02 mm (2.44 mm in CFD simulations) in its circular section and 1 mm in height; the corresponding interfacial area was 50.6 ± 0.18 cm$^2$·cm$^{-3}$ (50.5 cm$^2$·cm$^{-3}$ in CFD simulations). In addition, the mathematical model is able to predict the fluid dynamics of the system for different operating conditions.

Fig. 7 demonstrates through computational fluid dynamics (CFD) simulations how the hold-up of the aqueous phase, AP, (between 30 and 70 %) affects the generation of droplets in the microdevice keeping

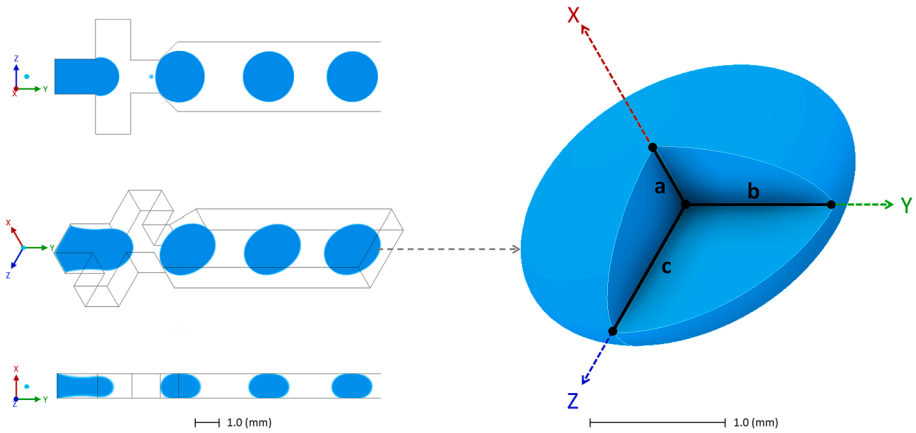


**Fig. 5.** 3D geometrical shape of the droplets generated in a microdevice with flow-focusing configuration simulated by CFD under the following operating conditions: $Q_{Aq} = 0.429$ ml·min$^{-1}$, $Q_{Org} = 1$ ml·min$^{-1}$, $\mu_{Aq} = 1$ cP, $\mu_{Org} = 1.6$ cP.

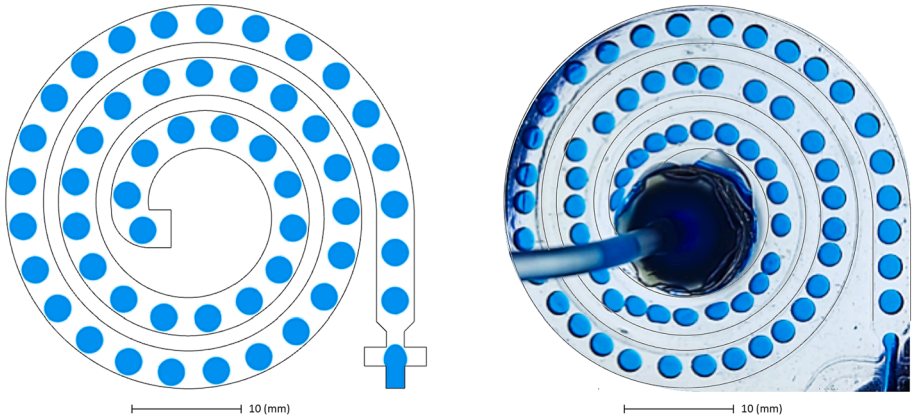


**Fig. 6.** Comparison of droplet generation fluid dynamics between CFD simulations in ANSYS Fluent® (on the left) and experiments (on the right), for the same conditions: $Q_{Aq} = 0.429$ ml·min$^{-1}$, $Q_{Org} = 1$ ml·min$^{-1}$, $\tau = 30$ s. Blue droplets and transparent fluid correspond to aqueous and organic phases respectively.

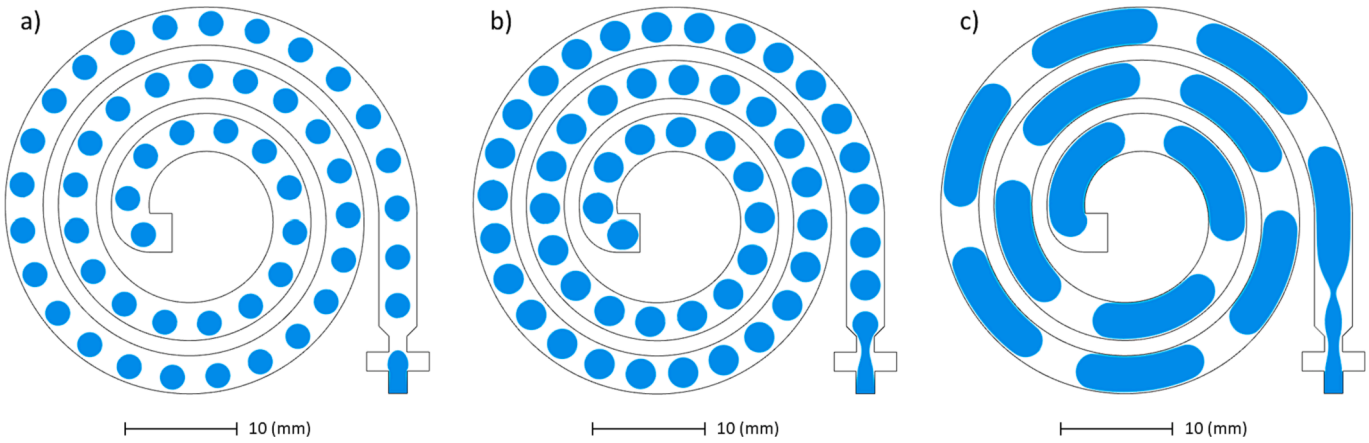


**Fig. 7.** Comparison of droplet generation fluid dynamics obtained through CFD simulations for the same residence time $\tau = 30$ s with different values of AP hold-up: a) 30 %, b) 50 %, and c) 70 %. Blue and transparent fluids correspond to the aqueous and organic phases respectively.

constant the residence time ($\tau = 30$ s). It can be seen that, for hold-ups of 30 % (Fig. 7.a) and 50 % (Fig. 7.b), spherical droplets are generated. However, with a hold-up of 70 % (Fig. 7.c), elongated droplets or slugs are produced. Regarding the frequency of droplets generation, it can be observed that it remains at 1.7 droplets·s$^{-1}$ for AP hold-ups of 30 % and 50 %, however, slug generation decreases this frequency to 0.5 droplets·s$^{-1}$.

In reactive multiphase microfluidic systems, the interfacial area between the fluid phases is a critical parameter in determining the contact between the reagents and, in the end, the performance of the solutes transport. The obtained results indicate that the highest interfacial area (50.5 cm$^2$·cm$^{-3}$ for a residence time of 30 s) is achieved with an AP hold-up of 30 %, followed by 33.2 cm$^2$·cm$^{-3}$ at 50 % AP hold-up. This is because, for the same droplet generation frequency, the highest

interfacial area inside the microdevice is obtained with smaller droplets. Furthermore, working with a slug flow is not convenient since a significant part of the slugs are in contact with the walls of the microdevice, resulting in a much lower specific area of 5.5 $cm^2 \cdot cm^{-3}$ between the fluid phases.

The fluid dynamics of the system also depend on the rheological properties of the fluid phases. It is therefore interesting to study how the viscosity of the liquid phases influences the size of the generated droplets. Fig. 8 shows the interfacial area of the droplets produced in the microfluidic device as a function of the viscosity of the continuous phase (keeping the viscosity of the dispersed phase $\mu_d = 1$ cP) for two different values of AP hold-up (30 % and 50 %). It can be seen that as the viscosity of the continuous phase (organic phase) increases, the size of the droplets generated in both conditions decreases, and therefore the interfacial area increases. This is because an increase in the viscosity of the continuous phase causes an increase in the stress tensor (Eq. (3)), improving the capacity of this phase to deform the dispersed one, and therefore causing an increase in the rate of the droplet breakage, producing droplets of smaller size. Moreover, this greater deformation capacity is more pronounced the higher the flow rate of the continuous phase is in relation to the dispersed one, and for this reason the variation of the interfacial area with an AP hold-up of 30 % is more sensitive (steeper curve) to the viscosity of the continuous phase compared to the results obtained with an AP hold-up of 50 %. Furthermore, there is a good agreement between the simulated curves with the mathematical model and the experimental data with an error of less than 10 % in terms of droplet size.

### 4.2. Microextraction

The potential advantages of droplet generation microdevices for carrying out very fast multiphase chemical reactions have been analysed through the performance of the reactive extraction and separation of rare earths, which are assumed to take place with very fast reaction rates. After the fluid dynamic analysis, the experiments were carried out with an aqueous phase hold-up of 30 % to increase the interfacial area between the phases, where the extraction reaction takes place.

The extraction of Dy(III) or La(III) by Cyanex® 572 from HCl solutions to the organic phase is represented through a cationic exchange reaction with the following stoichiometry [38]:

$$M^{3+} + 3\overline{(HA)_2} \leftrightarrow \overline{M(HA_2)_3} + 3H^+ \quad \text{(R1)}$$

where $M^{3+}$ represents the rare earth elements (Dy(III) and La(III)), $(HA)_2$ stands for the dimer of Cy-572 in Shellsol® D70 and the bars represent the organic phase species.

According to previous references [38], the equilibrium constant "$K_c$" of (R1) can be simplified and expressed by the mass action law Eq. (11),

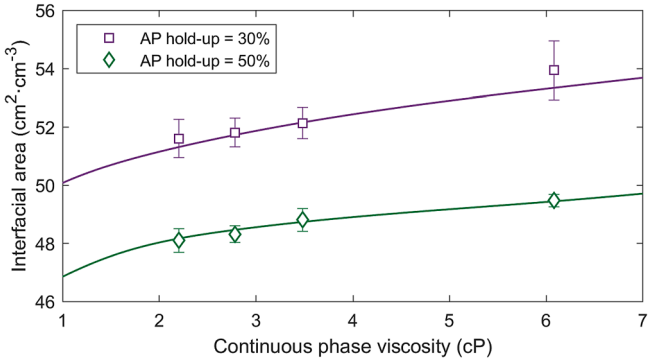


**Fig. 8.** Interfacial area of droplets (calculated by Eq. (10)) as function of the continuous phase viscosity for two different values of AP hold-up, at $Q_{Aq}$ = 0.429 ml·min$^{-1}$, $Q_{Org}$ = 1 ml·min$^{-1}$, $\tau$ = 30 s. Dots and lines represent experimental and simulated data respectively.

where "$K_c$" is also the ratio between the kinetic constant of the direct reaction "$k_f$" and the kinetic constant of the reverse reaction "$k_b$", as follows:

$$K_c = \frac{k_f}{k_b} = \frac{\overline{[M(HA_2)_3]} \cdot [H^+]^3}{[M^{3+}] \cdot [(HA)_2]^3} \quad (11)$$

Experimental data were fitted to the linearised expression of Eq. (11), Fig. 9, obtaining a dimensionless $K_c$ value of 1.5.

The extraction of rare earths by Cyanex® 572 has been reported to follow a pseudo first order kinetic equation [39], with respect to the rare earth elements "$M^{3+}$" and the complex species "$M(HA_2)_3$", as expressed in Eq. (12).

$$-\frac{dC_{M^{3+}}}{dt} = k_f \cdot C_{M^{3+}} - k_b \cdot C_{M(HA_2)_3} \quad (12)$$

where "$k_f$" and "$k_b$" are the observed kinetic constants of the direct and reverse reactions ($s^{-1}$), respectively, and "$C$" refers to the concentration of the reagents (mol·m$^{-3}$).

For simplicity, the concentrations of the extractant "$(HA)_2$" and of the protons "$H^+$", which are kept constant during the experiments under the conditions studied, are included in the values of the apparent kinetic constants. This way, the direct kinetic constant "$k_f$" was estimated from the experimental results, using Aspen Custom Modeler® (Aspen Custom Modeler V11, Aspen Technology Inc., Bedford, MA, USA) parameter estimation tool, obtaining values of $k_f = 0.37$ $s^{-1}$ and $k_b = 0.24$ $s^{-1}$.

In order to analyse the performance of REEs extraction and separation in a microfluidic device with droplet generation by CFD simulations, the influence of the mesh quality on the simulated results of dysprosium extraction was first studied. A structural mesh network was optimised for the microfluidic device to reduce the computational time and to improve the accuracy of the results. More details on the mesh quality (Fig. S5) can be found in the supplementary material.

Fig. 10 shows the microfluidic extraction of dysprosium from the aqueous to the organic phase (with 0.1 M and 0.001 M of HCl and 20 % v/v of Cy-572) as function of the residence time. It is observed that the microfluidic system is able to extract a significant amount of the Dy concentration (92 %, calculated with Eq. (8)) within a residence time of 30 s. Increasing the pH of the aqueous phase favours both the equilibrium and the extraction kinetics. This behaviour is consistent with the extraction reaction (R1) [38]; according to Eqs. (11) and (12), the variation in the proton concentration in the aqueous phase affects both the equilibrium (Le Châtelier's principle) and the extraction kinetics, reaching 92 % of the dysprosium extracted from the aqueous phase at pH 3 in only 10 s of residence time (3 times faster compared to the results at pH 1). Therefore, the low concentration of protons in the aqueous phase causes an increase in the rate of rare earths extraction, intensifying the microextraction process.

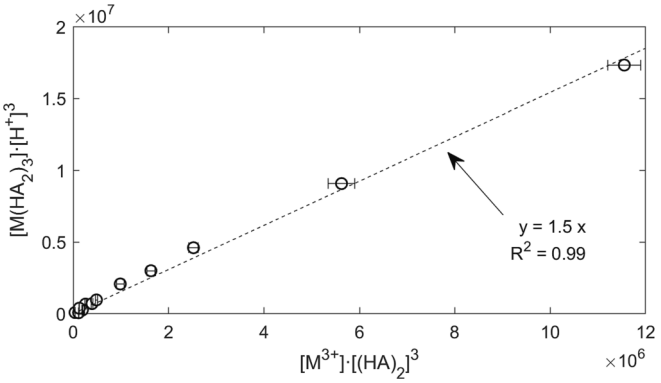


**Fig. 9.** Equilibrium constant study for dysprosium extraction at pH = 1 by Cyanex® 572 extractant at 21 ± 3 °C.

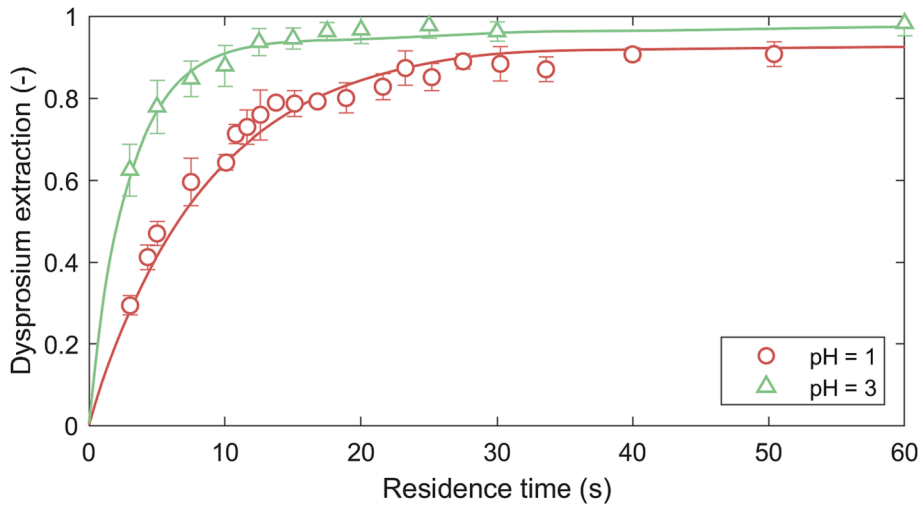


**Fig. 10.** Influence of pH on dysprosium extraction at different residence times from the HCl aqueous solution to the Cy-572 extractant organic phase at 22 ± 2 °C in the microdevice shown in Fig. 4. Dots and lines represent experimental and simulated data respectively.

Thus, the extraction of rare earths in microfluidic devices provide very promising results due to the high extraction achieved in very short residence times. This fast extraction process is enhanced due to the influence of the droplet characteristics; as the interfacial area increases, the contact area between the fluid phases increases and the distance that the dysprosium molecules must travel before reaching the reaction plane is shortened. For this reason, the time required to achieve 80 % REE extraction in this work's microdevice is 18 s; for similar extraction percentages the time required in a CSTR was 4 min [40] and in a SLM system it increased to 4 h [33].

This excellent performance in the extraction of Dy is mainly attributed to the efficient passive mixing of each phase due to the geometry of the microdevice and the high value of interfacial area. Fig. 11 shows CFD simulated internal flow patterns at different shear planes of the microdevice with a residence time of 30 s. Passive mixing inside the microdevice is caused by two factors; on the one hand, the curved parts of the spiral geometry cause passive mixing in both phases, induced by the formation of Dean vortices. These vortices create a secondary motion that develops as a pair of counter-rotating cells in the curved parts of the device. This phenomenon is characterised by the Dean number (De) and is calculated by the following equation:

$$De = \frac{\sqrt{\frac{1}{2}(inertial\ forces)(centripetal\ forces)}}{(viscous\ forces)} = Re\sqrt{\frac{d_h}{2r_c}} \tag{13}$$

where "*Re*" is the Reynolds number (-), "$d_h$" is the hydraulic diameter of the micro-channel (m) and "$r_c$" is the curvature radius of the channel (m).

On the one hand, this dimensionless number is influenced by the flow rate used in each individual experiment (different residence times between 3 and 60 s have been studied) which determines the Reynolds number, and on the other hand, for each experiment there is a range of Dean numbers because spirals have infinite curvature radius ($r_c$) between 3.4 and 17.9 mm. Consequently, this resulted in a range of Dean numbers between 0.4 and 1.0 for a residence time of 60 s whereas for a residence time of 3 s the Dean number varies from 8.7 to 19.8. Thus, the mixing efficiency is enhanced at lower residence times, but the chemical molecules have less time to interact and react with each other.

Therefore, the spiral curves have a positive effect on the performance

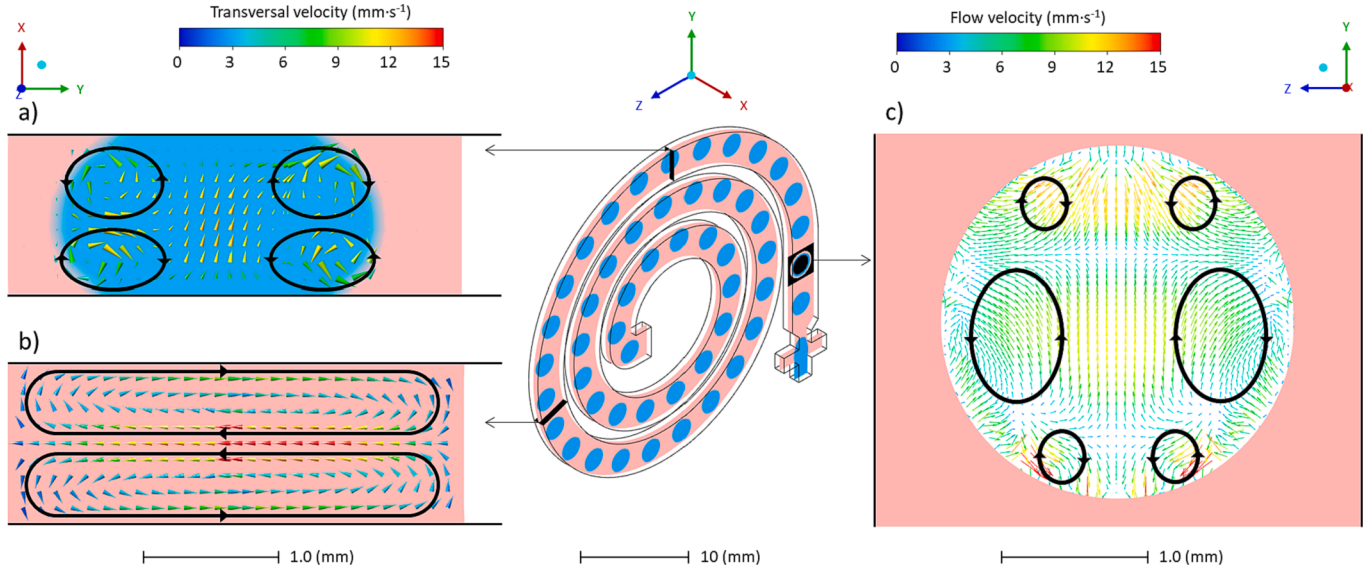


**Fig. 11.** CFD simulation of the flow internal pattern, a) in the dispersed phase, b) in the continuous phase; in both cases transversal sections of curved parts are represented, and c) in the dispersed phase within the droplet in the central plane. Simulation conditions were: $Q_{Aq}$ = 0.429 ml·min$^{-1}$, $Q_{Org}$ = 1 ml·min$^{-1}$, τ = 30 s.

of the microdevice, favouring the mass transport in the dispersed phase (Fig. 11.a), inducing the generation of 4 centrosymmetric vortices, and in the continuous phase (Fig. 11.b), generating two symmetrical vortices, reducing the diffusion limitation in both phases and thus decreasing the thickness of the boundary layer between the fluid phases, characteristic of systems flowing in laminar regime. On the other hand, the generation of vortices within the droplets (Fig. 11.c) is also critical [41]; the droplet is dragged by the continuous phase inside the microdevice, causing the generation of different velocities in the dispersed phase. The fluid at the droplet centreline flows in the same direction as the droplet motion, producing symmetrical recirculation regions around the centreline. Complex flow patterns also occur at each end of the droplet, resulting in an overall secondary flow that homogenises the concentration of species within the droplet. This has a direct effect on the extraction performance of this type of microfluidic device.

In order to quantify the difference in the performance, the extraction of dysprosium was simulated as a function of residence time for 3 different cases; first, the extraction of dysprosium was simulated in the spiral microdevice described in Materials and methods section, the dimensions of which are shown in Fig. S2. Second, the extraction of dysprosium was simulated in a microdevice with the same dimensions as described above, but with straight geometry as the only difference, so that the influence of curved parts on the extraction performance can be quantified. Finally, the extraction of dysprosium over time was simulated without considering the effects of the curves or the mixing caused by the dragging of droplets. For this purpose, the extraction of Dy was simulated in a motionless identical droplet.

Fig. 12 shows the results of the 3 simulation runs; it is observed that with a straight geometry, 80 % of Dy is extracted in 30 s of residence time, while with the spiral geometry the same extraction percentage is achieved in only 16.5 s. Consequently, the inclusion of geometries with curved parts leads to an increase in the extraction yield, being 1.8 times faster extraction in a spiral microdevice compared to the straight geometry. Furthermore, if we focus on the results obtained with a motionless droplet, it can be observed that the extraction performance in this case is significantly slower than that obtained with motion droplets, due to the diffusion limitation of Dy from the interior of the droplet to reach the L-L interphase, where it reacts with Cy-572. For this reason, after 30 s, only 61 % of the dysprosium is extracted in motionless droplets, requiring 90 s to reach 80 % extraction, 3 times more than in the straight microreactor, so the vortices generated inside the droplets by the drag force of the continuous phase on the dispersed one are also important. Therefore, the shape of the microdevice is key to achieve an efficient microextraction process, and as previously reported in literature [4,42,43], the incorporation of curves in the microdevice geometry significantly increases the performance of the process, which is more noticeable at high residence times, where the influence of the mixture becomes more important than the reaction rate. Other authors, such as Kolar et al. [44] compared the throughput of conventional bulk and microfluidic REEs extraction, starting from a 0.1 M REEs solution at pH 0.7 and using an organic phase constituted of a solution of 33 % v/v Cyanex® 572 in Shellsol® D70. They carried out the bulk extraction by stirring both phases with an impeller, while the solvent microextraction experiments were conducted in Y-Y microdevices, duplicating the extraction yield (defined as in Eq. (8)) compared to macroscale results. In order to compare these results with the ones obtained in this work under similar operating conditions, we have defined an enhancement factor (ε), calculated as the dimensioned dysprosium extraction rate divided by the specific interfacial area (S/V) of the system, observing that our microdevice is 2.8 times more efficient than the one used by Kolar E., as shown in Table 2.

The difference in the performance between the two microdevices is mainly due to the difference in the geometry, where the curved parts of the spiral geometry provide a higher efficiency of the passive mixing for both phases due to vortex generation, compared to a Y-Y device without curves in which this phenomenon does not occur.

Once it has been proved that the microextractors constitute useful and intensified devices to extract REEs, their performance in the separation of a binary rare earth system has been tested. Considering that REEs are typically classified in two groups according to the ionic radius [45], LREEs (Light Rare Earth Elements) or HREEs (Heavy Rare Earth Elements), in order to address this stage, in this work two REEs have been selected from each of the former categories; lanthanum, as representative of the LREEs group, and dysprosium, which belongs to the HREEs category and whose mixture is an industrial eluent of great interest in its separation and recovery of these elements [31].

Extraction experiments, which were carried at pH 1 in the aqueous phase (to minimise La extraction (pH < 1.2) [46] and facilitate the separation of dysprosium and lanthanum), 20 % v/v concentration of Cyanex® 572 extractant and 0.68 mM concentration for both REEs ($Dy^{3+}$ and $La^{3+}$), yielded the results displayed in Fig. 13. Based on the extraction curves, it can be highlighted that the considered setup would yield a high separation for the binary system (dysprosium-lanthanum). Indeed, with a residence time of 20 s, approximately 80 % of dysprosium

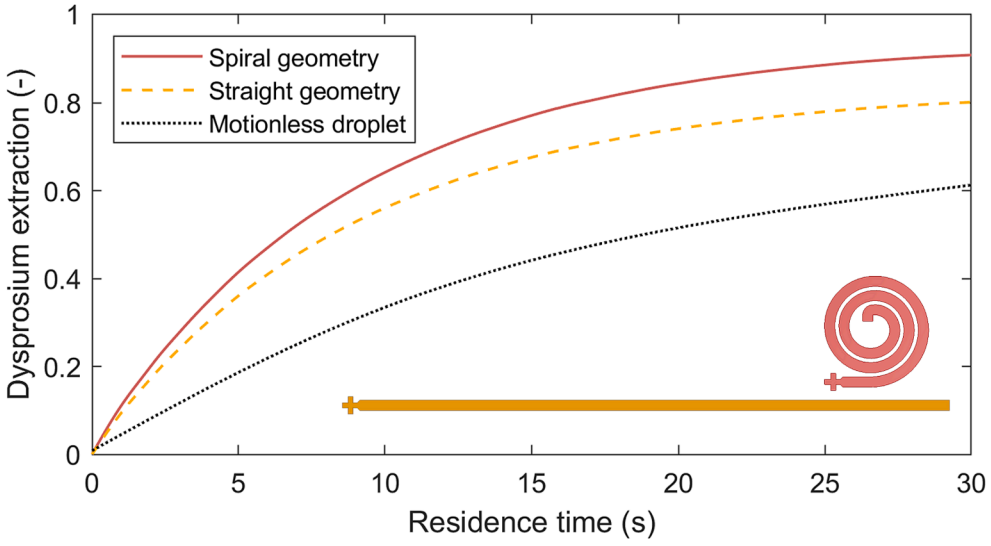


**Fig. 12.** Dysprosium extraction at different residence times from the HCl aqueous solution at pH = 1 to the Cy-572 extractant organic phase at 22 °C in different microdevice geometries with the same dimensions. Solid, dashed and dotted lines represent spiral shape, straight geometry and motionless droplet respectively.

**Table 2**
Comparison of the Dy extraction results obtained by Kolar E. [44] with those obtained in this work.

| Research (-) | τ (s) | $[Cy\text{-}572]_0$ (% v/v) | $[H^+]_0$ (mmol·L$^{-1}$) | $[REE]_0$ (mmol·L$^{-1}$) | $[REE]_{Ext}$ (mmol·L$^{-1}$) | S/V (mm$^{-1}$) | ε (mm$^{-1}$·min$^{-1}$) |
|---|---|---|---|---|---|---|---|
| Kolar E. Bulk impeller | 10 | 33 | 200 | 100 | 28 | 7 | 0.24 |
| Kolar E. Y-Y Microdevice | 10 | 33 | 200 | 100 | 59 | 14 | 0.25 |
| This work Spiral shape | 10 | 20 | 100 | 0.68 | 0.44 | 5.5 | 0.71 |

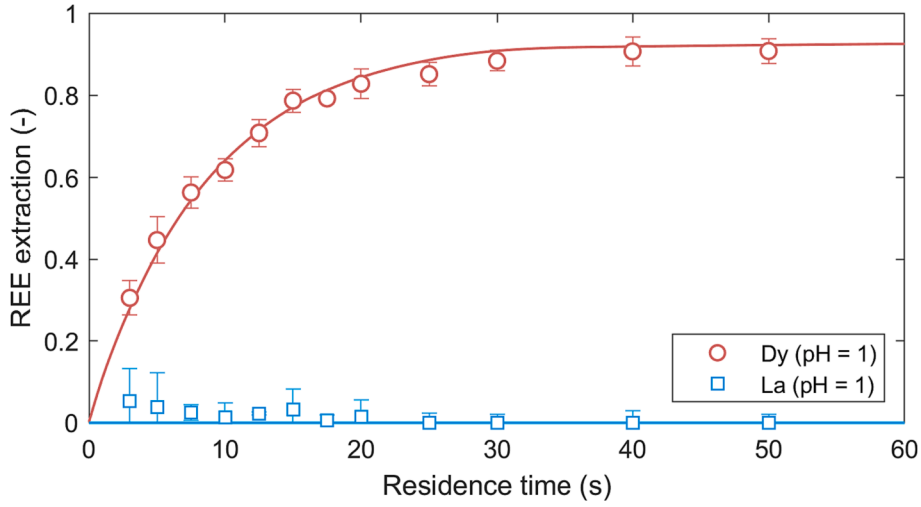


**Fig. 13.** Extraction curves for the mixture Dysprosium-Lanthanum at pH = 1 by Cyanex® 572 extractant at 22 ± 2 °C. Dots and lines represent experimental and simulated data, respectively.

would be extracted, due to the high interfacial area (58.4 cm$^2$·cm$^{-3}$) caused by the generated droplets, while the extraction of lanthanum would be practically null (less than 3 % of lanthanum extracted). To achieve the extraction of lanthanum from the aqueous phase, an additional extraction step is needed, the pH of the aqueous solution must be increased (pH = 3) so that the REE can be extracted by Cy-572 [46].

The behaviour represented in Fig. 13 is consistent with the expected outcomes from an acidic extractant as Cyanex® 572. These reagents extract by their conjugated bases, with extraction intensifying as the atomic number of the REE increases, corresponding to decreasing ionic radii and reinforcing the coordination strengths between Cyanex® 572 and REE [38,47]. This remarkable result of a separation factor of 175.9 (τ = 20 s) outcome is in good agreement with other results published in literature, calculated as:

$$\beta = \frac{\frac{C^0_{Dy}-C_{Dy}}{C_{Dy}}\cdot\frac{V_{Aq}}{V_{Org}}}{\frac{C^0_{La}-C_{La}}{C_{La}}\cdot\frac{V_{Aq}}{V_{Org}}} = \frac{C_{La}\cdot\left(C^0_{Dy}-C_{Dy}\right)}{C_{Dy}\cdot\left(C^0_{La}-C_{La}\right)} \tag{14}$$

where, "$C^0$" is the initial REE (Dy or La) concentration in the aqueous phase before extraction, "$C$" the REE concentration after extraction in the aqueous medium and "$V$" the volume of the aqueous (Aq) and organic (Org) phases.

For instance, El-Hefny et al. [38] reported, a considerably high separation factor of 156.3 for a binary mixture of REE obtained under similar operating conditions. Therefore, the microfluidic system is ideal to evaluate this type of separation, due to the possibility of generating monodispersed droplets through the flow-focusing geometry, increasing

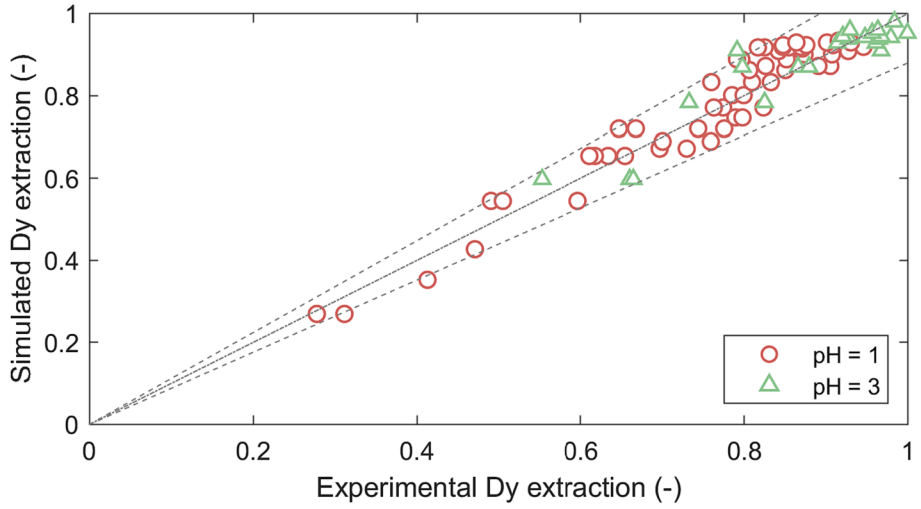


**Fig. 14.** Parity plot of dysprosium extraction with a ± 12 % error (grey dashed lines) between experimental values and the mathematical model simulations.

the interfacial area between phases and promoting passive mixing inside the droplets, and at the same time reducing the limitation to mass transport rate, overall enhancing the efficiency of the process; in this work, for the operational conditions, 90 % of dysprosium was extracted within 30 s of residence time and a high separation factor of $\beta = 279.3$.

Furthermore, using computational fluid dynamic (CFD) techniques with Ansys Fluent®, the fluid dynamics, mass transfer and chemical reaction kinetics of the microfluidic system have been solved simultaneously obtaining a good agreement between simulated data and experimental results, concluding that the mathematical model predicts the system with an error less than 12 % in 93 % of the cases (Fig. 14). This model represents an advanced tool for the design of multiphase reactive systems at the microscale that, in the specific case of droplet generation, allows the discrimination and selection of the fluid dynamics and geometry of the system that maximises the reaction target, i.e., extraction yield and selectivity in liquid–liquid reactive extractions.

## 5. Conclusions

The main result of this work is to advance knowledge in the design of high-performance microfluidic devices for multiphase liquid–liquid reactions by understanding and exploiting the advantageous characteristics of microdroplet generation. To this end, a predictive CFD model has been developed to assist in the microdroplet generation strategy, the design of the microfluidic device and the influence of operational variables on the reactive extraction of REEs.

After fabrication of the microfluidic device via additive manufacturing using 3D printing techniques, the spiral geometry with droplet generation by flow-focusing configuration allows the size and shape of the generated droplets to be controlled by various parameters such as the viscosity of the phases or the variation of the feed flow rates (AP hold-up), thus obtaining a multiphase system with a high interfacial area. In addition, the passive mixing induced in the dispersed phase inside the droplets by the dragging phases and in both phases by the Dean vortices generated in the spiral curve, provides a high-performance microfluidic system ideal for reactive extraction processes.

The experimental assessment of the model simulated results has been accomplished working with the extractive separation of a binary mixture of rare earth elements, dysprosium and lanthanum, that was fed to the microdevice as a dispersed phase according to the conditions selected from the simulation runs; an organic phase constituted of 20 % v/v of Cyanex® 572 as extractant dissolved in Shellsol® D70 was fed as a continuous phase. Under the operating conditions, the interfacial area achieved by the droplets was of 58.4 $cm^2 \cdot cm^{-3}$; working at pH = 1 90 % of dysprosium was successfully extracted in 30 s of residence time, whereas the extraction of lanthanum could be neglected, thus achieving a high separation factor of 279.3.

Thus, this work reports a valuable tool to assist in the design and fabrication of microfluidic devices for the development of dispersive liquid–liquid extractive reactions. A CFD mathematical model, which takes into account the integrated analysis of the fluid dynamics for multiphase systems, the mixing of the reactants within the microdevice and the interfacial reaction rate, has been developed and experimentally assessed; this tool allows the prediction of the performance under different operating conditions and facilitates the decision making on the process conditions for heterogeneous liquid–liquid reactions.

## CRediT authorship contribution statement

**Christian Fernández-Maza:** Writing – review & editing, Writing – original draft, Methodology, Investigation, Formal analysis, Data curation. **Gloria González-Lavín:** Writing – review & editing, Writing – original draft, Methodology, Investigation, Data curation. **Lucía Gómez-Coma:** Writing – review & editing, Writing – original draft, Supervision, Methodology, Conceptualization. **Marcos Fallanza:** Writing – review & editing, Writing – original draft, Supervision, Methodology. **Inmaculada Ortiz:** Writing – review & editing, Supervision, Resources, Project administration, Funding acquisition, Conceptualization.

## Declaration of competing interest

The authors declare that they have no known competing financial interests or personal relationships that could have appeared to influence the work reported in this paper.

## Data availability

Data will be made available on request.

## Acknowledgements

Financial assistance from the Project PDC2022-133122-I00 funded by MCIN/AEI /10.13039/501100011033 and the European Union Next Generation EU/PRTR is gratefully acknowledged. G. González-Lavín also thanks the FPU postgraduate research grant FPU21/03297 funded by MCIN/AEI/ 10.13039/501100011033 and ESF+. The authors thank Dr Gerardo Prieto from the University of Santiago de Compostela for the interfacial tension measurements.

## Appendix A. Supplementary data

Supplementary data to this article can be found online at https://doi.org/10.1016/j.cej.2024.150136.

## References

[1] OECD Economic Outlook, Interim Report March 2022: Economic and Social Impacts and Policy Implications of the War in Ukraine, OECD, Paris, 2022. https://doi.org/10.1787/4181d61b-en.
[2] J. Gómez-Pastora, C. González-Fernández, M. Fallanza, E. Bringas, I. Ortiz, Flow patterns and mass transfer performance of miscible liquid-liquid flows in various microchannels: Numerical and experimental studies, Chem. Eng. J. 344 (2018) 487–497, https://doi.org/10.1016/j.cej.2018.03.110.
[3] G.M. Whitesides, The origins and the future of microfluidics, Nature 442 (2006) 368–373, https://doi.org/10.1038/nature05058.
[4] C. Fernández-Maza, M. Fallanza, L. Gómez-Coma, I. Ortiz, Performance of continuous-flow micro-reactors with curved geometries. Experimental and numerical analysis, Chem. Eng. J. 437 (2022), https://doi.org/10.1016/j.cej.2022.135192.
[5] M.B. Plutschack, B. Pieber, K. Gilmore, P.H. Seeberger, The hitchhiker's guide to flow chemistry, Chem. Rev. 117 (2017) 11796–11893, https://doi.org/10.1021/acs.chemrev.7b00183.
[6] M.N. Kashid, D.W. Agar, Hydrodynamics of liquid-liquid slug flow capillary microreactor: flow regimes, slug size and pressure drop, Chem. Eng. J. 131 (2007) 1–13, https://doi.org/10.1016/j.cej.2006.11.020.
[7] S. Waelchli, P. Rudolf von Rohr, Two-phase flow characteristics in gas-liquid microreactors, Int. J. Multiph. Flow. 32 (2006) 791–806, https://doi.org/10.1016/j.ijmultiphaseflow.2006.02.014.
[8] C.G. Fernández, J.G. Pastora, A. Basauri, M. Fallanza, E. Bringas, J.J. Chalmers, I. Ortiz, Continuous-flow separation of magnetic particles from biofluids: how does the microdevice geometry determine the separation performance? Sensors (switzerland). 20 (2020) https://doi.org/10.3390/s20113030.
[9] R.K. Thomas, E. Nickerson, J.F. Simons, P.A. Jänne, T. Tengs, Y. Yuza, L. A. Garraway, T. LaFramboise, J.C. Lee, K. Shah, K. O'Neill, H. Sasaki, N. Lindeman, K.K. Wong, A.M. Borras, E.J. Gutmann, K.H. Dragnev, R. DeBiasi, T.H. Chen, K. A. Glatt, H. Greulich, B. Desany, C.K. Lubeski, W. Brockman, P. Alvarez, S. K. Hutchison, J.H. Leamon, M.T. Ronan, G.S. Turenchalk, M. Egholm, W.R. Sellers, J.M. Rothberg, M. Meyerson, Sensitive mutation detection in heterogeneous cancer specimens by massively parallel picoliter reactor sequencing, Nat. Med. 12 (2006) 852–855, https://doi.org/10.1038/nm1437.
[10] S. Kundu, A.S. Bhangale, W.E. Wallace, K.M. Flynn, C.M. Guttman, R.A. Gross, K. L. Beers, Continuous flow enzyme-catalyzed Polymerization in a microreactor, J. Am. Chem. Soc. 133 (2011) 6006–6011, https://doi.org/10.1021/ja111346c.
[11] E. Mousset, Interest of micro-reactors for the implementation of advanced electrocatalytic oxidation with boron-doped diamond anode for wastewater treatment, Curr. Opin. Electrochem. 32 (2022) 100897, https://doi.org/10.1016/j.coelec.2021.100897.
[12] F. Jamal, G. Jean-Sébastien, P. Maël, P. Edmond, R. Christian, Gold nanoparticle synthesis in microfluidic systems and immobilisation in microreactors designed for the catalysis of fine organic reactions, Microsyst. Technol. 18 (2012) 151–158, https://doi.org/10.1007/s00542-011-1369-9.

[13] M.J. Lima, A.M.T. Silva, C.G. Silva, J.L. Faria, N.M. Reis, Selective photocatalytic synthesis of benzaldehyde in microcapillaries with immobilized carbon nitride, Chem. Eng. J. 430 (2022) 132643, https://doi.org/10.1016/j.cej.2021.132643.
[14] H. Breisig, M. Schmidt, H. Wolff, A. Jupke, M. Wessling, Droplet-based liquid–liquid extraction inside a porous capillary, Chem. Eng. J. 307 (2017) 143–149, https://doi.org/10.1016/j.cej.2016.08.024.
[15] H. Song, J.D. Tice, R.F. Ismagilov, A microfluidic system for controlling reaction networks in time, Angew. Chemie Int. Ed. 42 (2003) 768–772, https://doi.org/10.1002/anie.200390203.
[16] A. Farahani, A. Rahbar-Kelishami, H. Shayesteh, Microfluidic solvent extraction of Cd(II) in parallel flow pattern: optimization, ion exchange, and mass transfer study, Sep. Purif. Technol. 258 (2021) 118031, https://doi.org/10.1016/j.seppur.2020.118031.
[17] J.C. Stachowiak, D.L. Richmond, T.H. Li, A.P. Liu, S.H. Parekh, D.A. Fletcher, Unilamellar vesicle formation and encapsulation by microfluidic jetting, Proc. Natl. Acad. Sci. u. s. a. 105 (2008) 4697–4702, https://doi.org/10.1073/pnas.0710875105.
[18] S.Y. Teh, R. Lin, L.H. Hung, A.P. Lee, Droplet microfluidics, Lab Chip. 8 (2008) 198–220, https://doi.org/10.1039/b715524g.
[19] L. Shang, Y. Cheng, Y. Zhao, Emerging droplet microfluidics, Chem. Rev. 117 (2017) 7964–8040, https://doi.org/10.1021/acs.chemrev.6b00848.
[20] C. Cramer, P. Fischer, E.J. Windhab, Drop formation in a co-flowing ambient fluid, Chem. Eng. Sci. 59 (2004) 3045–3058, https://doi.org/10.1016/j.ces.2004.04.006.
[21] P. Zhu, L. Wang, Passive and active droplet generation with microfluidics: a review, Lab Chip. 17 (2017) 34–75, https://doi.org/10.1039/C6LC01018K.
[22] T. Thorsen, R.W. Roberts, F.H. Arnold, S.R. Quake, Dynamic pattern formation in a vesicle-generating microfluidic device, Phys. Rev. Lett. 86 (2001) 4163–4166, https://doi.org/10.1103/PhysRevLett.86.4163.
[23] S.L. Anna, N. Bontoux, H.A. Stone, Formation of dispersions using “flow focusing” in microchannels, Appl. Phys. Lett. 82 (2003) 364–366, https://doi.org/10.1063/1.1537519.
[24] A.M. Ibrahim, J.I. Padovani, R.T. Howe, Y.H. Anis, Modeling of droplet generation in a microfluidic flow-focusing junction for droplet size control, Micromachines 12 (2021) 1–11, https://doi.org/10.3390/mi12060590.
[25] M. Mastiani, S. Seo, B. Riou, M. Kim, High inertial microfluidics for droplet generation in a flow-focusing geometry, Biomed. Microdevices. 21 (2019) 1–12, https://doi.org/10.1007/s10544-019-0405-x.
[26] C.X. Zhao, L. He, S.Z. Qiao, A.P.J. Middelberg, Nanoparticle synthesis in microreactors, Chem. Eng. Sci. 66 (2011) 1463–1479, https://doi.org/10.1016/j.ces.2010.08.039.
[27] EUROPEAN COMMISSION, Critical Raw Materials Resilience: Charting a Path towards greater Security and Sustainability, (2020). https://eur-lex.europa.eu/legal-content/EN/TXT/HTML/?uri=CELEX:52020DC0474&from=EN (accessed November 3, 2022).
[28] D.S. Sholl, R.P. Lively, Seven chemical separations to change the world, Nature. 532 (2016) 435–437, https://doi.org/10.1038/532435a.
[29] K.P. Nichols, R.R. Pompano, L. Li, A.V. Gelis, R.F. Ismagilov, Toward mechanistic understanding of Nuclear reprocessing chemistries by quantifying lanthanide solvent Extraction kinetics via microfluidics with constant Interfacial area and rapid mixing, J. Am. Chem. Soc. 133 (2011) 15721–15729, https://doi.org/10.1021/ja206020u.
[30] H. Zhang, H. Wang, X. Luo, D.Y.C. Leung, Q. Pang, H. Xu, L. Zhang, J. Xuan, Toward a mechanistic understanding of microfluidic droplet-based extraction and separation of lanthanides, Chem. Eng. J. 356 (2019) 673–679, https://doi.org/10.1016/j.cej.2018.09.043.
[31] Unpublished confidential document, (n.d.).
[32] D.W. Green, R.H. Perry, Perry’s chemical engineers’ handbook, 7th ed., McGraw-Hill, New York, 2003.
[33] S. Pavon, M. Kutucu, M.T. Coll, A. Fortuny, A.M. Sastre, Comparison of cyanex 272 and cyanex 572 for the separation of neodymium from a Nd/Tb/Dy mixture by pertraction, J. Chem. Technol. Biotechnol. 93 (2018) 2152–2159, https://doi.org/10.1002/jctb.5458.
[34] S. Chemicals, ShellSol D70, Tech. Datasheet ShellSol D70 (2016).
[35] K. Miyabe, R. Isogai, Estimation of molecular diffusivity in liquid phase systems by the wilke-chang equation, J. Chromatogr. a. 1218 (2011) 6639–6645, https://doi.org/10.1016/j.chroma.2011.07.018.
[36] D.R. Lide, S.R. Data, E.A. Board, G. Baysinger, S. Chemistry, C.E. Library, L. I. Berger, R.N. Goldberg, B. Division, H.V. Kehiaian, K. Kuchitsu, G. Rosenblatt, D. L. Roth, D. Zwillinger, CRC handbook of chemistry and physics, CRC Press, New York, 2004.
[37] V. Saggiomo, A.H. Velders, Simple 3D printed scaffold-removal method for the fabrication of intricate microfluidic Devices, Adv. Sci. 2 (2015) 1–6, https://doi.org/10.1002/advs.201500125.
[38] N.E. El-Hefny, M.S. Gasser, S.S. Emam, W.H. Mahmoud, H.F. Aly, Comparative studies on Y(III) and Dy(III) extraction from hydrochloric and nitric acids by cyanex 572 as a novel extractant, J. Rare Earths. 36 (2018) 1342–1350, https://doi.org/10.1016/j.jre.2018.04.012.
[39] C.A. Launiere, A.V. Gelis, High precision droplet-based microfluidic determination of americium(III) and lanthanide(III) solvent extraction separation kinetics, Ind. Eng. Chem. Res. 55 (2016) 2272–2276, https://doi.org/10.1021/acs.iecr.5b04691.
[40] M. Raji, H. Abolghasemi, J. Safdari, A. Kargari, Selective extraction of dysprosium from acidic solutions containing dysprosium and neodymium through emulsion liquid membrane by cyanex 572 as carrier, J. Mol. Liq. 254 (2018) 108–119, https://doi.org/10.1016/j.molliq.2017.11.058.
[41] X. Chao, F. Xu, C. Yao, T. Liu, G. Chen, CFD simulation of internal flow and mixing within droplets in a T-junction microchannel, Ind. Eng. Chem. Res. 60 (2021) 6038–6047, https://doi.org/10.1021/acs.iecr.1c00800.
[42] T.Y. Chen, P. Desir, M. Bracconi, B. Saha, M. Maestri, D.G. Vlachos, Liquid-liquid microfluidic flows for ultrafast 5-hydroxymethyl furfural extraction, Ind. Eng. Chem. Res. 60 (2021) 3723–3735, https://doi.org/10.1021/acs.iecr.0c05759.
[43] M.R. Asrami, N.N. Tran, K.D.P. Nigam, V. Hessel, Solvent extraction of metals: role of ionic liquids and microfluidics, Sep. Purif. Technol. 262 (2021) 118289, https://doi.org/10.1016/j.seppur.2020.118289.
[44] E. Kolar, R.P.R. Catthoor, F.H. Kriel, R. Sedev, S. Middlemas, E. Klier, G. Hatch, C. Priest, Microfluidic solvent extraction of rare earth elements from a mixed oxide concentrate leach solution using cyanex® 572, Chem. Eng. Sci. 148 (2016) 212–218, https://doi.org/10.1016/j.ces.2016.04.009.
[45] A. Jordens, Y.P. Cheng, K.E. Waters, A review of the beneficiation of rare earth element bearing minerals, Miner. Eng. 41 (2013) 97–114, https://doi.org/10.1016/j.mineng.2012.10.017.
[46] CYTEC, CYANEX® 572 Product Data Sheet, (2013).
[47] H. Nie, Y. Wang, Y. Wang, Z. Zhao, Y. Dong, X. Sun, Recovery of scandium from leaching solutions of tungsten residue using solvent extraction with cyanex 572, Hydrometall. 175 (2018) 117–123, https://doi.org/10.1016/j.hydromet.2017.10.026.